The Astrophysical Journal Letters, 875:L14 (7pp), 2019 April 20 https://doi.org/10.3847/2041-8213/ab1654

Carnegie Supernova Project-II: Using Near-infrared Spectroscopy to Determine the Location of the Outer ^{56}Ni in Type Ia Supernovae*

C. Ashall[1], E. Y. Hsiao[1], P. Hoeflich[1], M. Stritzinger[2], M. M. Phillips[1,3], N. Morrell[3], S. Davis[1], E. Baron[2,4,5], A. L. Piro[6], C. Burns[6], C. Contreras[3], L. Galbany[7], S. Holmbo[2], R. P. Kirshner[8,9], K. Krisciunas[10], G. H. Marion[11], D. J. Sand[12], M. Shahbandeh[1], N. B. Suntzeff[13], and F. Taddia[2,14]

[1] Department of Physics, Florida State University, Tallahassee, FL 32306, USA; Chris.Ashall@gmail.com
[2] Department of Physics and Astronomy, Aarhus University, Ny Munkegade 120, DK-8000 Aarhus C, Denmark
[3] Carnegie Observatories, Las Campanas Observatory, 601 Casilla, La Serena, Chile
[4] Homer L. Dodge Department of Physics and Astronomy, University of Oklahoma, 440 W. Brooks, Rm. 100, Norman, OK 73019-2061, USA
[5] Hamburger Sternwarte, Gojenbergsweg 112, D-21029 Hamburg, Germany
[6] Observatories of the Carnegie Institution for Science, 813 Santa Barbara Street, Pasadena, CA 91101, USA
[7] PITT PACC, Department of Physics and Astronomy, University of Pittsburgh, Pittsburgh, PA 15260, USA
[8] Gordon and Betty Moore Foundation, 1661 Page Mill Road, Palo Alto, CA 94304, USA
[9] Harvard-Smithsonian Center for Astrophysics, 60 Garden Street, Cambridge, MA 02138, USA
[10] George P. and Cynthia Woods Mitchell Institute for Fundamental Physics & Astronomy, Texas A&M University, Department of Physics, 4242 TAMU, College Station, TX 77843, USA
[11] University of Texas at Austin, 1 University Station C1400, Austin, TX 78712-0259, USA
[12] Department of Astronomy/Steward Observatory, 933 North Cherry Avenue, Rm. N204, Tucson, AZ 85721-0065, USA
[13] George P. and Cynthia Woods Mitchell Institute for Fundamental Physics & Astronomy, Texas A&M University, Department of Physics and Astronomy, 4242 TAMU, College Station, TX 77843, USA
[14] The Oskar Klein Centre, Department of Astronomy, Stockholm University, AlbaNova, SE-106 91 Stockholm, Sweden
Received 2019 January 22; revised 2019 March 26; accepted 2019 April 2; published 2019 April 16

Abstract

We present the *H*-band wavelength region of 37 postmaximum light near-infrared spectra of three normal, nine transitional, and four subluminous type Ia supernovae (SNe Ia), extending from +5 days to +20 days relative to the epoch of *B*-band maximum. We introduce a new observable, the blue-edge velocity, $v_{\rm edge}$, of the prominent Fe/Co/Ni-peak *H*-band emission feature, which is quantitatively measured. The $v_{\rm edge}$ parameter is found to decrease over subtype ranging from around −14,000 km s^{-1} for normal SNe Ia, to −10,000 km s^{-1} for transitional SNe Ia, down to −5000 km s^{-1} for the subluminous SNe Ia. Furthermore, inspection of the +10 ± 3 days spectra indicates that $v_{\rm edge}$ is correlated with the color-stretch parameter, s_{BV}, and hence with peak luminosity. These results follow the previous findings that brighter SNe Ia tend to have ^{56}Ni located at higher velocities as compared to subluminous objects. As $v_{\rm edge}$ is a model-independent parameter, we propose it can be used in combination with traditional observational diagnostics to provide a new avenue to robustly distinguish between leading SNe Ia explosion models.

Key words: supernovae: general

1. Introduction

Type Ia supernovae (SNe Ia) are the thermonuclear explosions of at least one carbon–oxygen white dwarf (WD) in a binary system. However, the exact nature of their progenitors and critical details of their explosion physics remain open questions.

The currently favored progenitor scenarios are the single degenerate scenario, where a WD accretes material from a nondegenerate companion star such as a H/He or red giant star (Whelan & Iben 1973; Livne 1990), and the double degenerate scenario, consisting of two WDs (Iben & Tutukov 1984). Within each progenitor scenario there are different explosion mechanisms and progenitor masses. However, it is still not clear if all of these scenarios are seen in nature, and if one of them dominates the production of SNe Ia in the universe. For a recent review on SNe Ia explosion scenarios, see Livio & Mazzali (2018).

SNe Ia follow a luminosity–width relation (LWR), where brighter objects have broader light curves (Phillips 1993). Subluminous, 1991bg-like (Filippenko et al. 1992) SNe Ia are located at the faint end of the LWR (e.g., Ashall et al. 2016a), and depending on the parameter combination used, subluminous SNe Ia have been proposed to be both part of a continuous distribution from normal SNe Ia (e.g., Hoeflich et al. 2017; Ashall et al. 2018; Burns et al. 2018) and from a distinct population (e.g., Stritzinger et al. 2006; Blondin et al. 2017; Dhawan et al. 2017; Scalzo et al. 2019).

At near-infrared (NIR) wavelengths SNe Ia are nearly standard candles and suffer from less systematic effects compared to the optical (Krisciunas et al. 2004; Wood-Vasey et al. 2008; Mandel et al. 2011; Kattner et al. 2012; Burns et al. 2014; Dhawan et al. 2018; Avelino et al. 2019). As a result current SNe Ia cosmology programs such as the *Carnegie Supernova Project II* (CSP-II; Phillips et al. 2019) have turned their attention toward longer wavelengths.

NIR spectroscopy offers a promising way to investigate the physics of SNe Ia, as it enable us to receive light from different depths in a supernova's atmosphere at the same epoch. This means a single NIR spectrum can simultaneously probe different burning regions in an SN Ia explosion. For normal-bright SNe Ia in the NIR, by a few days past maximum light,[15] there is no well-defined photosphere, and line blanketing dominates the opacity. In the region where there are lines, this opacity

* This Letter includes data gathered with the 6.5 m *Magellan* Telescopes located at Las Campanas Observatory, Chile.

[15] Throughout this Letter, phases (in days) are given with respect to time of rest-frame *B*-band maximum.

provides a quasi-continuum that is formed at relatively large radii. Conversely, in areas with few lines there is less opacity, enabling much deeper regions of the ejecta to be visible.

One wavelength region of interest coincides with the *H*-band where, between maximum light and +10 days, a complex iron-peak emission feature emerges due to allowed transitions located above the photosphere (Kirshner et al. 1973; Wheeler et al. 1998; Höflich et al. 2002; Marion et al. 2009; Hsiao et al. 2013). Previous work has found a correlation between the strength of this feature and the color-stretch parameter (Hsiao et al. 2013). Moreover, with a limited sample, Hsiao (2009) found an indication of a correlation between the velocity of this feature and light-curve shape. This iron-peak feature consists of a blend of many Fe II/Co II/Ni II allowed emission lines. The Fe and Co in these epochs are produced through the radioactive decay of ^{56}Ni. To first order, the luminosity of a supernova is dependent on the amount of ^{56}Ni synthesized in the explosion, where less luminous objects produce smaller amounts of ^{56}Ni (e.g., Arnett 1982; Stritzinger et al. 2006; Mazzali et al. 2007).

A primary objective of the CSP-II was to obtain a large sample of NIR spectra of SN Ia (Hsiao et al. 2019). In this work, we use a subset of these spectra to examine the *H*-band iron-peak feature in transitional and subluminous SNe Ia. Transitional objects are a link between normal-bright SNe Ia and the subluminous, 1991bg-like population (see, e.g., Pastorello et al. 2007; Hsiao et al. 2015; Ashall et al. 2016a, 2016b; Gall et al. 2018). Transitional SNe Ia are characterized by having (i) fast declining light curves, with $\Delta m_{15}(B) > 1.6$ mag,[16] (ii) a secondary *i*-band NIR maxima that peaks after the time of *B*-band maximum, (iii) and no strong Ti II absorption at 4400 Å.

Here, we suggest that the highest blue-edge velocity ($v_{\rm edge}$) of the iron-peak feature represents the outer edge of ^{56}Ni in the SNe Ia explosion. In an accompanying paper (Ashall et al. 2019) we compare $v_{\rm edge}$ to explosion models, and demonstrate it is a measurement of the specific kinetic energy in SNe Ia. We also show that $v_{\rm edge}$ is a quantification of the outer ^{56}Ni abundance in the ejecta. $v_{\rm edge}$ measures the point in velocity space where $X_{\rm Ni}$ falls to of order 0.03–0.10. Therefore, $v_{\rm edge}$ is a direct probe of the sharp transition between the incomplete and complete Si-burning regions in the ejecta.

Finally, we note that although the light-curve decline-rate parameter—$\Delta m_{15}(B)$—has successfully been used to calibrate the luminosity of SNe Ia, it is degenerate when dealing with subluminous and transitional objects. This is because, for the least luminous SNe Ia, the inflection point in the *B*-band light curve occurs prior to +15 days (Phillips 2012). Therefore, throughout the following work we characterize the properties of SNe Ia light curves with the color-stretch s_{BV} parameter. s_{BV} is a dimensionless parameter defined as the time difference between *B*-band maximum and the reddest point in the $B - V$ color curve divided by 30 days, where typical SNe Ia have $s_{BV} \approx 1$ (Burns et al. 2014).

2. Observational Sample

The selection criteria for the sample were set such that the SNe Ia were transitional or subluminous (i.e., they had $s_{BV} < 0.8$), and have at least one NIR spectrum, between +5 and +20 days, as these are the phases when it is predicted that the Fe/Co/Ni emission occurs (Marion et al. 2009), and is when the *H*-band break appears in the spectroscopic data. There were 12 SNe Ia that met these criteria from the CSP-II data set. The subluminous SN 1999by ($s_{BV} = 0.44$ (Höflich et al. 2002) and the normal SN 2011fe ($s_{BV} = 0.95$), SN 2014J ($s_{BV} = 1.05$), and ASASSN-14lp ($s_{BV} = 1.084$) (Hsiao et al. 2013; Pereira et al. 2013; Marion et al. 2015) were also used in the analysis. The basic properties of these SNe are presented in Table 1.

Optical spectra near maximum light of our sample (eight of which are unpublished) are plotted in Figure 1. A summary of the optical spectra can be found in Table 1. The three SNe Ia plotted in red show the typical characteristic of subluminous SNe Ia, a strong Ti II absorption feature at ∼4400 Å. The other SNe Ia have a higher ionization state and are classical transitional objects, except for SN 2011fe, SN 2014J, and ASASSN-14lp which are normal-bright SNe Ia. We note that SN 2013ay was classified from an NIR spectrum (Hsiao et al. 2013), has a light-curve shape consistent with a subluminous SNe Ia and an $s_{BV} = 0.46 \pm 0.05$, but does not have optical spectra. The unpublished CSP-II photometry of all the supernovae was checked, and the SNe Ia that were spectroscopically subluminous events were found to have small, but barely visible, secondary *i*-band maximum. Due to a lack of premaximum light-curve coverage, for the subluminous SNe Ia it was not possible to determine the *i*-band maximum relative to the *B*-band, except for SN 2015bo, which peaked in the *i* band before the *B*-band.

There are 37 NIR spectra of the 16 SNe Ia in the sample, 18 of which are unpublished (see Table 1 for details). Most of the spectra were observed with the FIRE spectrograph on the *Magellan* Baade telescope at Las Campanas Observatory, the other unpublished spectra were observed with SpeX on the NASA Infrared Telescope Facility (IRTF), Gemini Near-InfraRed Spectrograph (GNIRS) on Gemini-North, and FLAMINGOS-2 on Gemini-South. The spectra were reduced and corrected for telluric features via the procedure described by Hsiao et al. (2019).

The full sample of the NIR spectra is plotted in Figure 2. Each spectrum is corrected to the rest-frame, labeled with the appropriate SN name and rest-frame time relative to maximum. The figure shows only the *H*-band region of each spectrum.[17]

3. Technique

Here we describe our method to measure $v_{\rm edge}$. As demonstrated in Figure 3, $v_{\rm edge}$ was measured by fitting the minimum of the region blueward of the iron-peak emission feature with a Gaussian profile. The fit is weighted by the observational flux uncertainty. The data were fitted over a ∼0.05 μm range around a central value, illustrated by the red lines in Figure 3. The continuum is defined as a straight line connecting the end points in this range and removed before the fit. The Gaussian fit was iterated, using the previous minimum of the Gaussian as the central point in the new fit, until convergence was met. This was done to ensure the continuum was properly removed. Convergence usually required ∼5 iterations. We also fit the data with a Moffat function. Using the Bayesian information criterion, and Akaike information

[16] $\Delta m_{15}(B)$ 1.6 is the difference in magnitude between maximum light and +15 days (Phillips 1993).

[17] The entire NIR wavelength range of these data will be presented in a future publication.

Table 1
The Properties of the SNe Ia and a log of the NIR and Optical Spectral Observations

SN	z	s_{BV}	$\Delta m_{15}(B)$ (mag)	T_{Bmax}[a] (JD−2,450,000)	T_{spec}[b] (JD−2,450,000)	Phase[c] (days)	v_{edge} (km s^{-1})	Instrument/Telescope
				NIR				
ASASSN-14lp	0.005	1.08 ± 0.05	0.85 ± 0.07	57015.3	57020.3	+5.0	−14,700 ± 100	F2/Gemini-S
					57025.3	+10.0	−13,700 ± 100	F2/Gemini-S
SN 2014J	0.0001	1.05 ± 0.086	1.05 ± 0.05	56689.75	56694.95	+5.2	−14,100 ± 200	Mt Abu
					56695.78	+6.0	−14,100 ± 100	Mt Abu (1)
					56696.93	+7.1	−13,900 ± 100	Mt Abu (1)
					56697.92	+8.1	−13,800 ± 100	Mt Abu (1)
					56699.84	+10.0	−13,400 ± 100	Mt Abu (1)
SN 2011fe	0.001	0.95 ± 0.01	1.21 ± 0.05	55813.93	55822.13	+8.2	−13,800 ± 600	GNIRS/Gemini-N
					55826.22	+12.3	−13,500 ± 100	GNIRS/Gemini-N
					55831.21	+17.3	−13,300 ± 100	GNIRS/Gemini-N
SN 2011jh	0.008	0.80 ± 0.01	1.46 ± 0.01	55931.06	55941.84	+10.69*	−13,300 ± 400	FIRE/Baade
SN 2013aj	0.009	0.78 ± 0.01	1.47 ± 0.01	56361.37	56371.72	+10.25*	−13,600 ± 300	FIRE/Baade
					56376.81	+15.30*	−12,300 ± 300	FIRE/Baade
PS1-14ra	0.028	0.77 ± 0.01	⋯	56724.54	56734.84	+10.01*	−13,000 ± 900	FIRE/Baade
					56741.82	+16.81*	−10,900 ± 2200	FIRE/Baade
ASASSN-15aj	0.011	0.76 ± 0.01	1.44 ± 0.02	57035.46	57050.64	+15.01*	−12,100 ± 500	FIRE/Baade
PSN-171[d]	0.020	0.71 ± 0.01	1.54 ± 0.02	57070.43	57088.82	+18.03*	−6700 ± 2000	FIRE/Baade
SNhunt281[e]	0.004	0.68 ± 0.01	1.56 ± 0.03	57112.67	57119.79	+7.09*	−12,200 ± 300	FIRE/Baade
					57124.72	+12.00*	−12,200 ± 900	FIRE/Baade
					57128.41	+15.74*	−7100 ± 100	GNIRS/Gemini-N
					57131.28	+18.71*	−7200 ± 100	Spex/IRTF
LSQ14ajn[f]	0.021	0.64 ± 0.01	1.74 ± 0.02	56734.73	56741.70	+6.83*	−12,400 ± 1200	FIRE/Baade
SN 2011iv	0.006	0.64 ± 0.01	1.74 ± 0.01	55906.08	55911.70	+5.58	−13,200 ± 200	FIRE/Baade
					55913.68	+7.55	−12,800 ± 200	FIRE/Baade
					55915.7	+9.60	−12,500 ± 200	SOFI/NTT
					55916.75	+10.60	−12,900 ± 200	FIRE/Baade
					55924.6	+18.50	−6300 ± 200	ISAAC/VLT
iPTF13ebh	0.013	0.61 ± 0.01	1.76 ± 0.02	56623.29	56630.0	+6.71	−12,100 ± 100	GNIRS/Gemini-N
					56635.58	+12.12	−10,600 ± 1800	FIRE/Baade
					56640.56	+17.04	−7200 ± 1000	FIRE/Baade
ASASSN-15ga	0.007	0.50 ± 0.03	2.13 ± 0.04	57115.88	57124.68	+8.74*	−6500 ± 1500	FIRE/Baade
SN 2015bo	0.016	0.47 ± 0.01	1.85 ± 0.02	57076.02	57088.86	+12.63*	−7000 ± 1300	FIRE/Baade
SN 2013ay	0.016	0.46 ± 0.05	⋯	56375.41	56383.84	+8.30*	−7700 ± 600	FIRE/Baade
					56385.91	+10.33*	−7800 ± 700	FIRE/Baade
SN 1999by	0.002	0.44 ± 0.01	1.90 ± 0.05	51308	51316	+8	−7600 ± 300	TIFKAM/Hiltner (2)
					51319	+11	−5500 ± 200	TIFKAM/Hiltner
					51322	+14	−5000 ± 300	TIFKAM/Hiltner
				Optical				
ASASSN-14lp	0.005	1.08 ± 0.05	0.85 ± 0.07	57015.3	57011	−4	⋯	FLWO-1.5 m / FAST (3)
SN 2014J	0.0001	1.05 ± 0.086	1.05 ± 0.05	56689.75	56692	+2	⋯	Frodospec/LT (4)
SN 2011fe	0.001	0.95 ± 0.01	1.21 ± 0.05	55813.93	55814	+0	⋯	SNIFS/UH 2.2m (5)
SN 2011jh	0.008	0.80 ± 0.01	1.46 ± 0.01	55931.06	55927	−4	⋯	B& C/Du Pont (6)
SN 2013aj	0.009	0.78 ± 0.01	1.47 ± 0.01	56361.37	56356	−5	⋯	EFOSC/NTT (7)
PS1-14ra	0.028	0.77 ± 0.01	⋯	56724.54	56728	+3	⋯	ALFOSC/NOT (6)
ASASSN-15aj	0.011	0.76 ± 0.01	1.44 ± 0.02	57035.46	57035	+0	⋯	MIKE Clay (6)
PSN-171[d]	0.020	0.71 ± 0.01	1.54 ± 0.02	57070.43	57068	−2	⋯	ALFOSC/NOT (6)
SNhunt281[e]	0.004	0.68 ± 0.01	1.56 ± 0.03	57112.67	57108	−5	⋯	ALFOSC/NOT (6)
LSQ14ajn[f]	0.021	0.64 ± 0.01	1.74 ± 0.02	56734.73	56729	−6	⋯	ALFOSC/NOT (6)
SN 2011iv	0.006	0.64 ± 0.01	1.74 ± 0.01	55906.08	55907	+1	⋯	STIS/*HST* (8)
iPTF13ebh	0.013	0.61 ± 0.01	1.76 ± 0.02	56623.29	56623	+0	⋯	DBSP/Palomar200 (9)
ASASSN-15ga	0.007	0.50 ± 0.03	2.13 ± 0.04	57115.88	57121	+5	⋯	ALFOSC/NOT (6)
SN 2015bo	0.016	0.47 ± 0.01	1.85 ± 0.02	57076.02	57079	+3	⋯	B& C/Du Pont (6)
SN 1999by	0.002	0.44 ± 0.01	1.90 ± 0.05	51308	51303	−5	⋯	FAST/FLWO (10)

Notes. The $\Delta m_{15}(B)$ values were obtained from a direct spline fit to the data, and the values of s_{BV} were obtained from the best fits from SNooPy.
[a] Time B-band maximum, calculated from the CSP-II light curves.
[b] Time of spectral observation.
[c] Phase of spectra in rest frame relative to B-band maximum.
[d] J13471211-2422171.
[e] SN 2015bp.
[f] SN 2014ah.
References. (1) Marion et al. (2015); (2) Höflich et al. (2002); (3) Shappee et al. (2016); (4) Ashall et al. (2014); (5) Pereira et al. (2013); (6) N. Morrell et al. (2019, in preparation); (7) Smartt et al. (2015); (8) Gall et al. (2018); (9) Hsiao et al. (2015); (10) Garnavich et al. (2004).

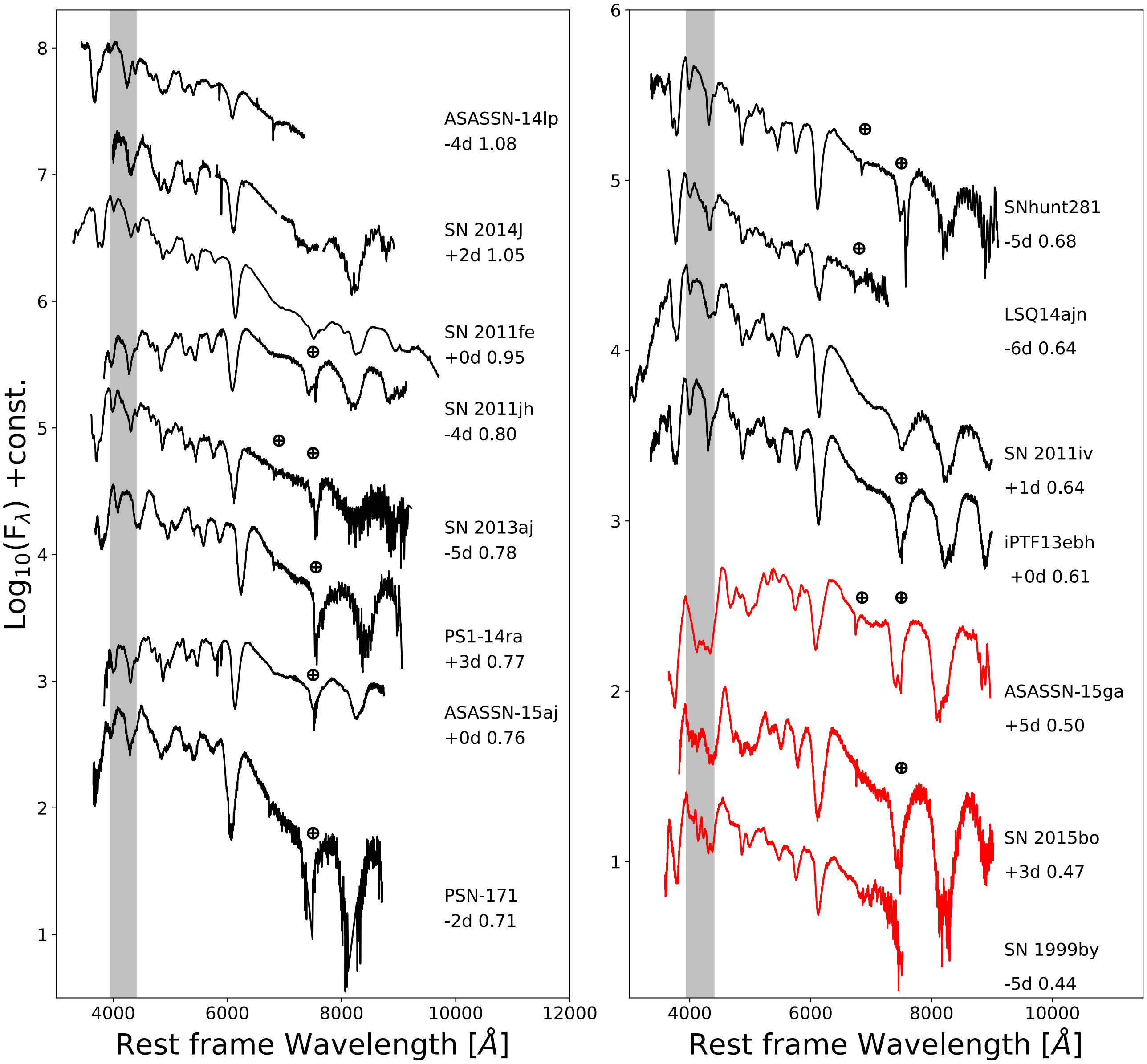

Figure 1. Rest-frame visual-wavelength spectra of the SNe used in this work. Their phase relative to maximum and as well as s_{BV} is plotted adjacent to each spectrum. The objects are plotted in order of s_{BV}, and those in red have strong Ti II absorption at 4400 Å. The gray vertical region highlights the Ti II 4400 Å feature. All of the spectra are from N. Morrell et al. (2019, in preparation), except for, ASASSN-14lp (Shappee et al. 2016), SN 2014J (Ashall et al. 2014), SN 2011fe (Pereira et al. 2013), SN 2011iv (Gall et al. 2018), iPTF13ebh (Hsiao et al. 2015), SN 1999by (Garnavich et al. 2004), and SN 2014ah (Yaron & Gal-Yam 2012). The telluric features in the spectra are marked.

criterion, it was found that a Gaussian function models the profile better than a Moffat function.

An accompanying uncertainty to our best-fit value of $v_{\rm edge}$ was determined by producing 100 realizations on a smoothed spectrum with noise added in at each pixel using a normal distribution with the standard deviation of the Gaussian matching the observed flux error, denoted by the light gray error region in the left panel of Figure 3. The flux errors of the FIRE spectra come from the standard deviation in flux of the multiple exposures necessary in NIR observations (Hsiao et al. 2019). This newly constructed spectrum was then measured over the same region and with the same fitting technique as the observed input spectrum. This was done for each realization to create an array of 100 velocity measurements for the given feature whose standard deviation was taken as the measurement error of $v_{\rm edge}$. If no error spectrum was available from the observations, an array of values was produced through subtracting the smoothed spectrum and the observations. The absolute value of these subtracted values were smoothed to generate a noise trend. This noise trend was used as a representation of the mean noise on the spectra and sampled back onto the smoothed spectra to produce another realization of the observed spectra. For each of the 100 realizations of the Gaussian fit discussed above, a different amount of noise was sampled from the noise trend back onto the smoothed spectra.

The iron-peak emission region is a multiplet of many allowed Fe/Co/Ni lines and not from an individual transition. As a result, the different components are sensitive to density and temperature, hence the ionization and excitation state in the center of the feature can differ. However, the Doppler shift of

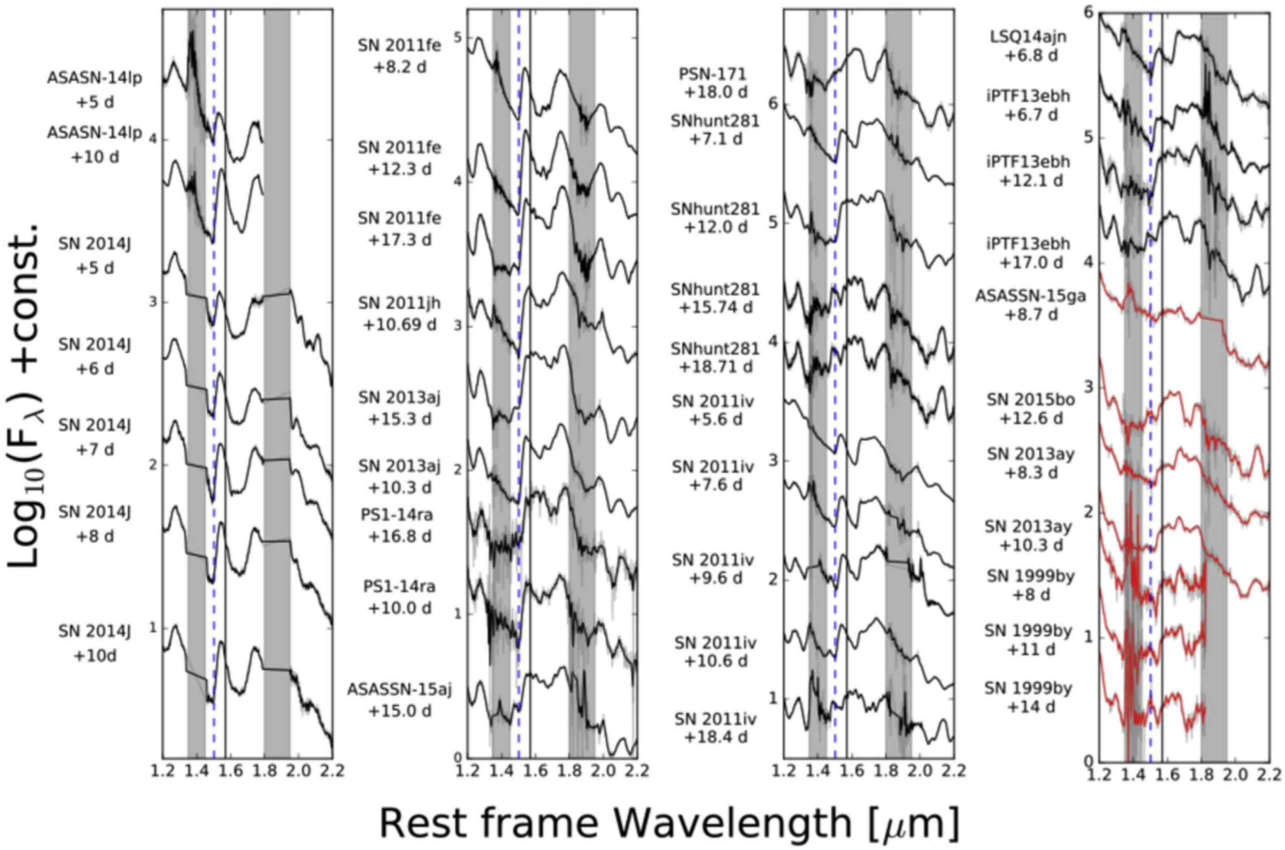

Figure 2. CSP-II SNe Ia NIR spectra used in this Letter, sorted by s_{BV}, where the objects get fainter from going from the top of the left panel to the bottom of the right panel. The name of each supernova and its time relative to B-band maximum is adjacent to each spectrum. The Gaussian smoothed ($\sigma = 2$) spectra are plotted in black and red and the unsmoothed spectra are underneath in gray. The vertical gray regions are the telluric bands in the NIR. The vertical black lines denote the rest wavelength of the 1.57 μm feature, and the dashed blue line corresponds to the same feature at $-13{,}000$ km s^{-1}.

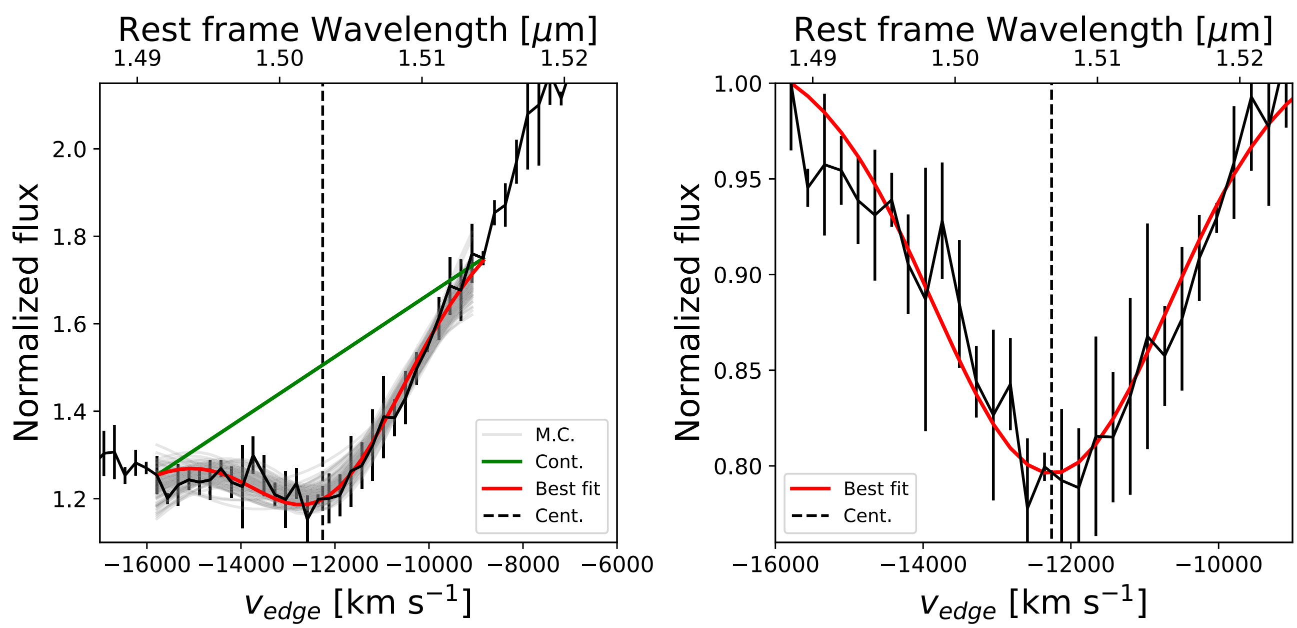

Figure 3. Example of how v_{edge} is determined using the $+7.09$ day spectrum of SNhunt281. Left panel: the continuum (green) determined from iteration from the Gaussian fit, the best Gaussian fit (red), the data (black solid), the central value of the Gaussian (black dashed), and the 100 Monte Carlo realizations (gray). The flux errors of the observations are provided as error bars. Right panel: the best Gaussian fit (red), the normalized data (black solid), and the central value of the Gaussian (black dashed) produced through the fitting process. The continuum from the left panel has been removed.

the highest energy (bluest edge) component is not sensitive to density and temperature. This is because it is a result of atomic physics. Therefore we use the outer edge of the feature to measure velocities, as this is a stable measurement. In this work we adopt 1.57 μm as the rest wavelength of the feature. This value was obtained by checking for the strongest lines from

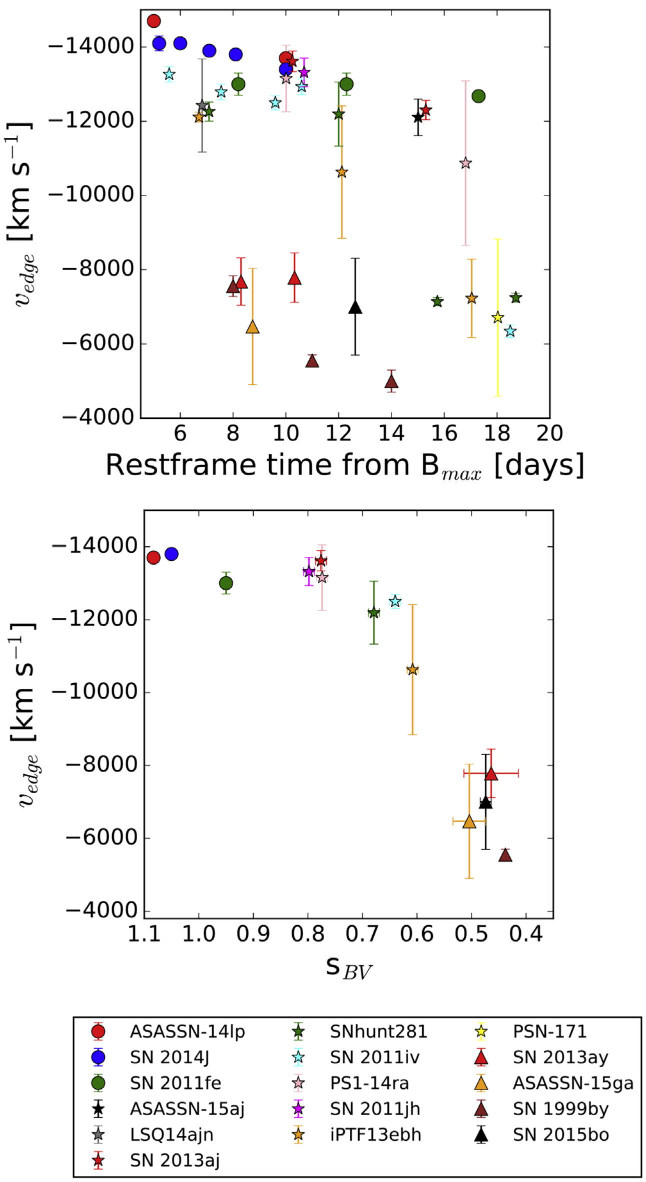

Figure 4. Top panel: $v_{\rm edge}$ as a function of rest-frame time from maximum. Bottom panel: the iron-peak outer velocity at +10 ± 3 days as a function of s_{BV}. For some objects the error bars are smaller than the marker sizes. Normal SNe Ia are marked by solid circle symbols, transitional SNe Ia are marked by star circle symbols, and subluminous SNe Ia are marked by solid triangle symbols.

non-LTE radiation transport models of normal and subluminous SNe Ia (Höflich et al. 2002; Hoeflich et al. 2017). However, if the rest wavelength of this feature were to be altered, it would just cause a systematic shift in the values and not change the trend.

4. Results

Using the method described above, $v_{\rm edge}$ was measured for each of the NIR spectra, and the results are presented in the top panel of Figure 4. Inspection of the measurements reveals that $v_{\rm edge}$ decreases over time for the majority of objects. The normal-bright ASASSN-14lp exhibits the highest velocities, reaching −14,700 ± 100 km s^{-1} on +5.2 days and later −13,700 ± 100 km s^{-1} on +10.0 days. Transitional objects exhibit slightly lower values of $v_{\rm edge}$, which then decrease rapidly. For example, SN 2011iv (Ashall et al. 2018; Gall et al. 2018) extends from $v_{\rm edge}$ = −13,200 ± 200 km s^{-1} at +5.6 days down to −6300 ± 200 km s^{-1} by +10 days. The least luminous SNe Ia have the lowest values of $v_{\rm edge}$, clustering around −6000 km s^{-1}. At +8 days SN 1999by has a $v_{\rm edge}$ of −7600 ± 300 km s^{-1} and by +14 days it drops to −5000 ± 300 km s^{-1}.

SNe Ia with a $v_{\rm edge}$ of ∼−10,000 km s^{-1} appear to be rare. However, SN 2011iv, SNhunt281, and iPTF13ebh are the only objects that rapidly drop over the time period examined. For example, iPTF13ebh exhibits a $v_{\rm edge}$ of −10,600 ± 1800 km s^{-1} at +12.12 days, but by +17.04 days it drops to −7200 ±1000 km s^{-1}.

In the bottom panel of Figure 4, we have plotted $v_{\rm edge}$ as a function of the color-stretch parameter s_{BV}. The points from the spectra at +10 ± 3 days were plotted because at later times the corresponding layers may become optically thin. Objects exhibiting larger s_{BV} values are found to also exhibit higher values of $v_{\rm edge}$. $v_{\rm edge}$ was found to range from ∼−14,000 km s^{-1} for normal-bright SNe Ia, to −10,500 km s^{-1} for transitional SNe Ia, and down to ∼−5000 km s^{-1} for subluminous SNe Ia. The correlation between s_{BV} and $v_{\rm edge}$ implies $v_{\rm edge}$ is also correlated with the peak luminosity of the SNe Ia, and hence the amount of ^{56}Ni produced during the explosion.

From our sample here it is not possible to rule out that there is bimodality in the data, where the subluminous SNe Ia cover a larger range in $v_{\rm edge}$ than the normal-bright SNe. However, photometric properties of SNe Ia, such as those from CSP-I, show a continuous distribution from normal to subluminous SNe Ia (Burns et al. 2018). This implies that the possible bimodal distribution seen in this work is produced by a small sample size, and the fact that transitional SNe Ia are rare. A Pearson correlation test of the points in the bottom panel of Figure 4 produced a correlation coefficient of −0.86.

5. Discussion

A measure of $v_{\rm edge}$ provides a constraint on the outer ^{56}Ni distribution in the ejecta. This is because the Fe/Co/Ni emission region is located at large radii in the SN atmosphere, is an isolated multiplet, and is not contaminated by lines from other elements. Furthermore, the highest energy Doppler shift of this region will correspond to the edge of the highest velocity emission, which is a measurement of the outer ^{56}Ni. $v_{\rm edge}$ is therefore a valuable tool to analyze the explosion physics of SNe Ia. For example, measuring $v_{\rm edge}$ for a large sample of SNe will probe the mixing of ^{56}Ni in the ejecta.

$v_{\rm edge}$ is a model-independent measurement, and a diagnostic of the location between the complete and incomplete Si-burning regions. It provides an indication of the effectiveness of the burning in the ejecta. Those objects that are brighter, and produce more ^{56}Ni, have experienced more effective burning. The exact details of this will be explored in an accompanying paper with respect to explosion models (Ashall et al. 2019). However, the results here are consistent with those found through nebular phase spectral modeling by Mazzali et al. (1998) who showed that less luminous objects have ^{56}Ni located at lower velocities. A similar result was also found by Botyánszki & Kasen (2017) who demonstrate, using nebular phase modeling, that a larger ^{56}Ni mass (and therefore SN luminosity) produces broader Fe lines in the ejecta.

Our results indicate that ^{56}Ni is located at lower velocities for less luminous SNe Ia, and may argue against very low-mass explosions (less than ∼$0.9M_\odot$) for the subluminous SNe Ia.

This is because, for the same ^{56}Ni mass, these very low-mass explosions tend to have the ^{56}Ni located at higher velocities compared to M_{Ch} explosions (e.g., Sim et al. 2010; Blondin et al. 2018). Finally, the fact that we see a relatively smooth distribution in v_{edge} as a function of light-curve shape implies that at least some SNe Ia at the faint end of the luminosity–width relationship may have a similar explosion mechanism to normal SNe Ia.

We thank our many colleagues for fruitful discussions, as well as Josh Simon, Povilas Palunas, and Mansi Kasliwal for providing telescope time. The work presented here has been supported in part by NSF awards AST-1008343 and AST-1613426 (PI: M.M.P.), AST-1613472 (PI: E.Y.H.), AST-1715133 (PI: P.H.), AST- 16113455 (PI: N.B.S.) and in part by a Sapere Aude Level II grant (PI: M.D. Stritzinger) from the Danish National Research Foundation (DFF). M.D. Stritzinger and S.H. are generously supported by a research grant (13261) from the VILLUM FONDEN. M.D. Stritzinger and E.B. acknowledge support from the Aarhus University Research Fund (AUFF) for a Sabbatical research grant. E.B. acknowledges partial support from NASA grant NNX16AB25G. Research by D.J.S. is supported by NSF grants AST-1821967, 1821987, 1813708, and 1813466. We thank the Mitchell Institute for Fundamental Physics and Astronomy for partial support. Based on observations obtained at the Gemini Observatory under program GS-2015A-Q-5 (PI: D.J.S.). Gemini is operated by the Association of Universities for Research in Astronomy, Inc., under a cooperative agreement with the NSF on behalf of the Gemini partnership: the NSF (United States), the National Research Council (Canada), CONICYT (Chile), Ministerio de Ciencia, Tecnología e Innovación Productiva (Argentina), and Ministério da Ciência, Tecnologia e Inovação (Brazil). D.J.S. is a visiting Astronomer at the Infrared Telescope Facility, which is operated by the University of Hawaii under contract NNH14CK55B with the National Aeronautics and Space Administration. Based in part on observations made with the Nordic Optical Telescope (P49-017, P50-015, and P51-006; PI: M.D. Stritzinger), operated by the Nordic Optical Telescope Scientific Association at the Observatorio del Roque de los Muchachos, La Palma, Spain, of the Instituto de Astrofisica de Canarias.

Facilities: Magellan: Baade (FIRE near-infrared echellette), *Magellan*: Clay (*Magellan* Inamori Kyocera Echelle), du Pont (Boller & Chivens spectrograph), Gemini:North (GNIRS near-infrared spectrograph), VLT (ISAAC), NTT (EFOSC), IRTF (SpeX near-infrared spectrograph), Hale (DBSP), Hiltner (TIFKAM), NOT (ALFOSC), UH:2.2m (SNIFS), FLWO:1.5m (FAST), *HST* (STIS), La Silla-QUEST.

ORCID iDs

C. Ashall https://orcid.org/0000-0002-5221-7557
M. Stritzinger https://orcid.org/0000-0002-5571-1833
M. M. Phillips https://orcid.org/0000-0003-2734-0796
N. Morrell https://orcid.org/0000-0003-2535-3091
E. Baron https://orcid.org/0000-0001-5393-1608
K. Krisciunas https://orcid.org/0000-0002-6650-694X
D. J. Sand https://orcid.org/0000-0003-4102-380X

References

Arnett, W. D. 1982, ApJ, 253, 785
Ashall, C., Hoeflich, P., Hsiao, E. Y., et al. 2019, arXiv:1904.01633
Ashall, C., Mazzali, P., Bersier, D., et al. 2014, MNRAS, 445, 4427
Ashall, C., Mazzali, P., Sasdelli, M., & Prentice, S. J. 2016a, MNRAS, 460, 3529
Ashall, C., Mazzali, P. A., Pian, E., & James, P. A. 2016b, MNRAS, 463, 1891
Ashall, C., Mazzali, P. A., Stritzinger, M. D., et al. 2018, MNRAS, 477, 153
Avelino, A., Friedman, A. S., Mandel, K. S., et al. 2019, arXiv:1902.03261
Blondin, S., Dessart, L., & Hillier, D. J. 2018, MNRAS, 474, 3931
Blondin, S., Dessart, L., Hillier, D. J., & Khokhlov, A. M. 2017, MNRAS, 470, 157
Botyánszki, J., & Kasen, D. 2017, ApJ, 845, 176
Burns, C. R., Parent, E., Phillips, M. M., et al. 2018, ApJ, 869, 56
Burns, C. R., Stritzinger, M., Phillips, M. M., et al. 2014, ApJ, 789, 32
Dhawan, S., Jha, S. W., & Leibundgut, B. 2018, A&A, 609, A72
Dhawan, S., Leibundgut, B., Spyromilio, J., & Blondin, S. 2017, A&A, 602, A118
Filippenko, A. V., Richmond, M. W., Branch, D., et al. 1992, AJ, 104, 1543
Gall, C., Stritzinger, M. D., Ashall, C., et al. 2018, A&A, 611, A58
Garnavich, P. M., Bonanos, A. Z., Krisciunas, K., et al. 2004, ApJ, 613, 1120
Hoeflich, P., Hsiao, E. Y., Ashall, C., et al. 2017, ApJ, 846, 58
Höflich, P., Gerardy, C. L., Fesen, R. A., & Sakai, S. 2002, ApJ, 568, 791
Hsiao, E. Y., Burns, C. R., Contreras, C., et al. 2015, A&A, 578, A9
Hsiao, E. Y., Marion, G. H., Morrell, N., et al. 2013, ATel, 4935, 1
Hsiao, E. Y., Marion, G. H., Phillips, M. M., et al. 2013, ApJ, 766, 72
Hsiao, E. Y., Phillips, M. M., Marion, G. H., et al. 2019, PASP, 131, 014002
Hsiao, Y. C. E. 2009, PhD thesis, Univ. Victoria, Canada
Iben, I., Jr., & Tutukov, A. V. 1984, ApJS, 54, 335
Kattner, S., Leonard, D. C., Burns, C. R., et al. 2012, PASP, 124, 114
Kirshner, R. P., Willner, S. P., Becklin, E. E., Neugebauer, G., & Oke, J. B. 1973, ApJL, 180, L97
Krisciunas, K., Suntzeff, N. B., Phillips, M. M., et al. 2004, AJ, 128, 3034
Livio, M., & Mazzali, P. 2018, PhR, 736, 1
Livne, E. 1990, ApJL, 354, L53
Mandel, K. S., Narayan, G., & Kirshner, R. P. 2011, ApJ, 731, 120
Marion, G. H., Höflich, P., Gerardy, C. L., et al. 2009, AJ, 138, 727
Marion, G. H., Sand, D. J., Hsiao, E. Y., et al. 2015, ApJ, 798, 39
Mazzali, P. A., Cappellaro, E., Danziger, I. J., Turatto, M., & Benetti, S. 1998, ApJL, 499, L49
Mazzali, P. A., Röpke, F. K., Benetti, S., & Hillebrandt, W. 2007, Sci, 315, 825
Pastorello, A., Mazzali, P. A., Pignata, G., et al. 2007, MNRAS, 377, 1531
Pereira, R., Thomas, R. C., Aldering, G., et al. 2013, A&A, 554, A27
Phillips, M. M. 1993, ApJL, 413, L105
Phillips, M. M. 2012, PASA, 29, 434
Phillips, M. M., Contreras, C., Hsiao, E. Y., et al. 2019, PASP, 131, 014001
Scalzo, R. A., Parent, E., Burns, C., et al. 2019, MNRAS, 483, 628
Shappee, B. J., Piro, A. L., Holoien, T. W.-S., et al. 2016, ApJ, 826, 144
Sim, S. A., Röpke, F. K., Hillebrandt, W., et al. 2010, ApJL, 714, L52
Smartt, S. J., Valenti, S., Fraser, M., et al. 2015, A&A, 579, A40
Stritzinger, M., Mazzali, P. A., Sollerman, J., & Benetti, S. 2006, A&A, 460, 793
Wheeler, J. C., Höflich, P., Harkness, R. P., & Spyromilio, J. 1998, ApJ, 496, 908
Whelan, J., & Iben, I., Jr. 1973, ApJ, 186, 1007
Wood-Vasey, W. M., Friedman, A. S., Bloom, J. S., et al. 2008, ApJ, 689, 377
Yaron, O., & Gal-Yam, A. 2012, PASP, 124, 668